

See discussions, stats, and author profiles for this publication at: <https://www.researchgate.net/publication/233761647>

Multitechnique Characterization of a Polyaniline–Iron–Carbon Oxygen Reduction Catalyst. The Journal of Physical Chemistry C 116 (30):16001–16013

ARTICLE in THE JOURNAL OF PHYSICAL CHEMISTRY C · AUGUST 2012

Impact Factor: 4.77 · DOI: 10.1021/Jp302396g

CITATIONS

60

READS

232

9 AUTHORS, INCLUDING:



Magali Ferrandon

Argonne National Laboratory

54 PUBLICATIONS 1,209 CITATIONS

SEE PROFILE



Deborah J. Myers

Argonne National Laboratory

100 PUBLICATIONS 2,883 CITATIONS

SEE PROFILE



Kateryna Artyushkova

University of New Mexico

147 PUBLICATIONS 1,650 CITATIONS

SEE PROFILE



Piotr Zelenay

Los Alamos National Laboratory

140 PUBLICATIONS 7,416 CITATIONS

SEE PROFILE

Multitechnique Characterization of a Polyaniline–Iron–Carbon Oxygen Reduction Catalyst

Magali Ferrandon,* A. Jeremy Kropf, and Deborah J. Myers

Chemical Sciences and Engineering Division, Argonne National Laboratory, Lemont, Illinois 60439, United States

Kateryna Artyushkova

Department of Chemical and Nuclear Engineering, 209 Farris Engineering Center, University of New Mexico, Albuquerque, New Mexico 87131, United States

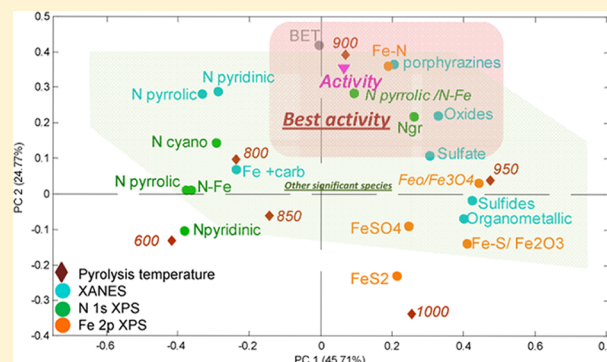
Ulrike Kramm and Peter Bogdanoff

Department of Solar Fuels and Energy Storage (E-I6), Helmholtz-Center Berlin for Materials and Energy, Hahn-Meitner-Platz 1, 14109 Berlin, Germany

Gang Wu, Christina M. Johnston, and Piotr Zelenay

Materials Physics and Applications Division, Los Alamos National Laboratory, Los Alamos, New Mexico 87545, United States

ABSTRACT: This paper summarizes a XANES, XPS, XRD, and Mössbauer study of an oxygen reduction reaction (ORR) catalyst obtained via a heat treatment of polyaniline, iron, and carbon black. The catalyst was characterized at several critical synthesis stages and following heat treatment at various temperatures. The effect of sulfur during the synthesis was also investigated. XANES linear combination fitting (XANES-LCF) was used to determine the speciation of iron using 16 iron standards. The highest ORR activity was measured with a catalyst heat-treated at 900 °C, with the largest Fe–N_x content, as determined by the XANES-LCF, also characterized by the highest microporosity. An absence or a reduction in the amount of a sulfur-based oxidant in the aniline polymerization was found to lead to an increase in the amount of iron carbide formed during the heat treatment and a decrease in the number of Fe–N₄ centers, thus attesting to an indirect beneficial role of sulfur in the catalyst synthesis. Using principal component analysis (PCA), a good correlation was found between the ORR activity and the presence of Fe–N_x structures.



INTRODUCTION

The slow kinetics of oxygen reduction reaction (ORR) at the cathode is a major contributor to the efficiency loss in the state-of-the-art polymer electrolyte fuel cells (PEFCs).¹ While platinum and its alloys remain the most active ORR catalysts, the high demand and low natural abundance of Pt are responsible for the high catalyst cost. To reduce the PEFC cost, numerous groups have focused their attention on developing catalysts based on metals with high natural abundance, such as Fe and Co. The effort was started with an early discovery by Jasinski of ORR catalysis by cobalt phthalocyanine.^{2,3} A particularly promising route to Fe- and Co-based catalysts, both in terms of activity and stability, is the heat treatment of carbon- and nitrogen-containing macrocycle compounds of these metals. Later studies replaced the expensive macrocycle precursors with a wide variety of common nitrogen-containing

chemicals (ammonia, acetonitrile, amines, etc.). It was believed that the heat treatment of almost any mixture of (1) nitrogen, (2) carbon, and (3) metal precursors will result in a material that is ORR-active; however, the degree of activity and durability depend greatly on the selection of precursors and synthesis chemistry. Recently, polyaniline (PANI), an aromatic heteroatom polymer, was discovered as an effective nitrogen–carbon template to generate high-performance non-precious group metal (non-PGM) ORR catalysts in PEFCs.^{4–8}

While it is commonly accepted that heat treatment is necessary to produce active and stable Fe- and/or Co-based electrocatalysts, the reported optimum heat-treatment temper-

Received: March 12, 2012

Revised: June 25, 2012

Published: June 25, 2012

ature varies with the synthesis conditions and precursors used. Typically, the highest electrocatalytic activity has been found with catalysts pyrolyzed between 500 and 700 °C, the approach arguably leading to the formation of Fe–N₄ centers as active ORR sites.^{9–11} However, the use of a heat treatment at higher temperatures has been at times found to be advantageous.^{9,10,12,13} At these higher temperatures, the active sites were proposed not to be Fe–N₄ centers^{10,14} but rather Fe–N_{2+x} centers, which showed higher activity than Fe–N₄.^{15,16} In a later work by the same group the FeN_{2+x} centers were specified as FeN₂₊₂ centers.¹⁷ While the heat treatment temperature at which the highest ORR activity is obtained depends on a specific catalyst, the improved stability is often associated with heat treatment at higher temperatures.^{18–20}

Several recent literature reviews have demonstrated the importance of elucidating the ORR active sites in this class of catalyst.^{1,21–24} This study is a follow-up on a previous effort in the development of PANI–Fe–C ORR catalyst at Los Alamos National Laboratory.^{7,8} The purpose of the study was to elucidate the identity of the active site in the PANI–Fe–C class of catalysts by correlating ORR activity with the catalyst morphology and chemical speciation as a function of variation in the catalyst preparation procedure, specifically heat treatment temperature and presence of sulfur-containing precursor. The main technique utilized in this study was X-ray absorption fine structure (XAFS) spectroscopy, which comprises X-ray absorption near-edge structure (XANES) and extended X-ray absorption fine structure (EXAFS) and enables the measurement of atomic structure, bonding characteristics, and oxidation state with elemental specificity. EXAFS has proven to be useful for studying a variety of ORR catalyst materials both *ex situ*^{10,25–29} and *in situ*.^{14,30–32} However, because of the multicomponent nature of this class of catalysts, an analysis of the EXAFS region of the XAFS spectra for the identity of the Fe nearest neighbors, coordination numbers, and bond lengths was not possible. In addition, EXAFS cannot discriminate between metal–oxygen and metal–nitrogen bonds.⁸ The XANES regions of the spectra were therefore utilized to determine the oxidation state and chemical speciation of iron by the comparison with the XANES region of 16 iron-containing standards using linear combination fitting (XANES-LCF). XANES-LCF is a standard technique for determining the composition of multicomponent samples and has been widely applied in the speciation of environmental samples.^{33–36} X-ray photoelectron spectroscopy (XPS) was used to quantify the near-surface Fe and N speciation (quaternary, graphitic, and pyrrolic) for the same set of catalysts. The results of these X-ray spectroscopies were complemented by surface area and pore size measurements using nitrogen adsorption analysis (BET), identification of the crystalline phases formed using X-ray diffraction (XRD), determination of the Fe content using inductively coupled plasma optical emission spectroscopy, and identification of the Fe species in the most active catalysts using Mössbauer spectroscopy. Fe-57 Mössbauer spectroscopy is a sensitive tool for characterizing iron-containing compounds and has been extensively used to correlate the ORR activity with the amount of Fe–N₄ centers.^{11,13,37,38} Principal component analysis (PCA) was used to correlate the chemical speciation obtained by XANES and XPS and the ORR activity.

■ EXPERIMENTAL SECTION

Catalyst Synthesis. A detailed description of the catalyst synthesis procedure was presented previously;⁷ thus, an

abbreviated version is given here. Ketjenblack EC 300J (KJ-300J) high-surface-area carbon was used as the support. The carbon black was pretreated in an aqueous HCl solution for 24 h to remove possible impurities. Aniline (2.0 mL) was first dispersed with acid-treated carbon black (0.4 g) in HCl solution (0.5 M). The suspension was kept below 10 °C while the oxidant, ammonium peroxydisulfate (APS, (NH₄)₂S₂O₈), and transition metal precursor (FeCl₃) were added. Hydrogen peroxide (H₂O₂) was used as an oxidant instead of APS to synthesize sulfur-free PANI–Fe–C catalysts. After continuous mixing for 24 h to allow PANI to uniformly combine with the carbon black particles, the suspension containing carbon, polymer, and transition metal was vacuum-dried using a rotary evaporator. The subsequent heat treatment was performed at temperatures ranging from 400 to 1000 °C in an inert atmosphere of nitrogen gas for 1 h. The heat-treated sample was acid-leached in H₂SO₄ (0.5 M) at 80 °C for 8 h to remove unstable and inactive species from the catalyst and then thoroughly washed in deionized water. In the final step, the catalyst was heat-treated again under the same conditions as those used in the first heat treatment but for 3 h instead of 1 h. For all catalysts investigated, one initial concentration of Fe precursor was used except for the Mössbauer samples, where two initial concentrations were used. The amount of Fe precursor required in the synthesis to give the highest activity and the most reproducible results was demonstrated to be 10 wt % in a previous study.⁸ Therefore, this amount of Fe was used in this work. Throughout the remainder of this report, the catalyst materials will be identified as PANI–Fe–C followed by “HT1” for the material obtained after the first heat treatment step, “AL1” for the material after the first acid-leaching step, and “HT2” for the material after the second heat treatment step (e.g., “PANI–Fe–C_HT1_AL1_HT2”). If the heat treatment temperature is not indicated, it is 900 °C.

RDE Testing. Rotating disk electrode (RDE) testing was performed using a CHI Electrochemical Station (Model 750b) in a conventional three-electrode cell at room temperature and at a disk rotation speed of 900 rpm. The catalyst loading was 0.6 mg cm^{−2} on a 0.2475 cm² glassy carbon electrode (PINE). A graphite rod and Ag/AgCl (3 M NaCl, 0.235 V vs RHE, a measured value) were the counter and reference electrodes, respectively. The ORR steady-state polarization curves were recorded in oxygen-saturated 0.5 M H₂SO₄ electrolyte with a potential step of 0.03 V and a holding time at each potential of 30 s. After 30 s, when the background capacitive current had passed, a steady-state value of the Faradaic current was measured.

X-ray Absorption Near-Edge Structure (XANES). X-ray absorption spectroscopy measurements at the Fe K-edge were carried out in either transmission or fluorescent mode at the 10-BM, 12-BM, and 20-BM beamlines at the Advance Photon Source at Argonne National Laboratory. The near-edge region of the XAFS spectra (7105–7155 eV) was fit using the linear combination algorithm of the Athena software (version 0.8.054) based on the IFEFFIT code,³⁹ to the spectra for a suite of Fe-containing standards. The total loading of Fe in the sample was measured using the XAFS edge step height in transmission mode. The edge step was measured by fitting a line through the pre-edge region and a second-order polynomial above the edge. The difference at the edge was compared to the difference in the tabulated Fe X-ray cross sections below the edge and above the edge.

Catalyst Surface Area. The catalyst surface area was determined by nitrogen adsorption using a Micromeritics ASAP 2010 instrument. Each sample was degassed by heating at 150 °C under vacuum prior to measuring the surface area. The five-point BET surface area was measured. Because the samples had significant microporosity, the surface area was also determined from the adsorption isotherm using nonlocal density functional theory (NLDFT) or quenched-solid density functional theory (QSFDFT) with a slit pore geometry (Quantachrome analysis software), depending on which model gave the best fit to each isotherm.

X-ray Diffraction. Crystalline phase compositions of PANI–Fe–C were determined by powder X-ray diffraction using a Siemens diffractometer 5000 operating with the following parameters: Cu K α radiation of 30 mA, 40 kV, K_{λ} = 0.154 06 nm, 2θ scanning range of 5°–80°, and a scan step size of 0.02°.

Inductively Coupled Plasma Optical Emission Spectroscopy. The Fe content of the catalyst samples was also determined using inductively coupled plasma optical emission spectroscopy (ICP-OES). This was accomplished by first removing the carbon component of the samples by dry-ashing the carbon at 700 °C and bringing the ash residue into solution for the analysis of Fe concentration using ICP-OES. The residue from the ignition of ~25 mg of sample was dissolved in 5 mL of deionized water (18 M Ω cm), 1 mL of concentrated, trace-metals-grade, hydrochloric acid (Fisher), and 1 mL of concentrated, trace-metals-grade nitric acid (Fisher). The residue was refluxed in the acid mixture for 3 h, which was adequate to completely dissolve the residue. The acid solution was then quantitatively diluted with deionized water and Fe concentration in the product solutions measured with a Perkin-Elmer Optima 3300 DV ICP-OES versus reference solutions prepared from commercial spectroscopic standards (Ultra Scientific, Kingstown, RI). The mass fraction of iron in each sample was calculated from the measured solution concentration, the known solution volume (50 mL), and the mass of the sample analyzed.

^{57}Fe Mössbauer. Mössbauer spectroscopy was used to characterize two catalysts obtained by heat treatment at 900 °C, acid leach, and a second heat treatment also at 900 °C. The samples had final Fe contents of ~3 wt % (Cat1) and 10 wt % (Cat2, “standard catalyst”). Each Mössbauer spectrum was recorded at room temperature (RT) using a 1024 multichannel analyzer equipped with a constant electronic drive system with triangular reference waveform (Halder Electronics, Germany). A $^{57}\text{Co}/\text{Rh}$ source was used, and velocity scale and isomer shift δ_{iso} were calibrated against natural iron (α -Fe-foil, 25 μm thick, 99.99% purity). The spectra were recorded in a velocity range of $\pm 4 \text{ mm s}^{-1}$. The spectroscopic data were analyzed with the program Recoil. For a better visualization of all contributions, the “standard catalyst” was also measured in a velocity range of $\pm 7 \text{ mm s}^{-1}$. The precursors were fitted with two doublets. In order to obtain a reasonable fit for both final catalysts, the inclusion of one singlet, three doublets, and three sextets was necessary.

X-ray Photoelectron Spectroscopy. Catalysts before and after heating at different temperatures were analyzed by XPS. The XPS spectra were acquired by a Kratos AXIS Ultra photoelectron spectrometer using a monochromatic Al K α source operating at 300 W. The base pressure of the spectrometer was 2×10^{-10} Torr, and the operating pressure was 2×10^{-9} Torr. Charge compensation was accomplished

using low-energy electrons. Standard operating conditions for good charge compensation were a –4.1 V bias voltage, a –1.0 V filament voltage, and a 2.1 A filament current. The reported XPS data represent averages from 3 areas per sample. The survey of each area was done first, followed by the recording of high-resolution spectra of C 1s, N 1s, S 2p, O 1s, and Fe 2p for all the samples. Au powder was put on each sample, and Au 4f spectra were acquired. Linear background was used for elemental quantification of C 1s, N 1s, S 2p, and O 1s spectra while Shirley background was used for Fe 2p spectra. Quantification utilized sensitivity factors provided by the manufacturer. All the spectra were charge-referenced to the Au 4f at 84 eV. Curve fitting was carried out using individual peaks of constrained width, position, and 70% Gaussian/30% Lorentzian line shape.

Principal Component Analysis. Principal component analysis (PCA) was used to determine the correlation between the speciation obtained by XANES and XPS, the ORR activity, the BET surface area, and the microporous surface area. The PCA of data was done with a help of PLS_Toolbox 6.0 for Matlab (eigenvector Research, I, PLS_Toolbox 6.0: Wenatchee, WA) using an autoscaling as the preprocessing option (mean centering and scaling to unit variance). PCA is a multivariate statistical analysis method allowing for classification of samples into groups. At its most fundamental level, PCA visualizes the difference between samples (captured in scores) and “explains” which variables (parameters) make samples different (captured in loadings). The first output from PCA is component coefficients or loadings, which are the coefficients of the linear combinations of the original variables that generate the principal components. The second output, scores, contains the coordinates of the original data in the new coordinate system. Biplots displaying both the loadings for each variable and the scores for each sample in a single plot for the PC1 and PC2 were produced to visualize the clustering of samples with respect to variables that were the most or least important for separating samples. Correlated variables and samples are located in the same quadrant on a biplot.

■ RESULTS AND DISCUSSION

XANES Spectra of Reference Compounds. Because of the large number of standard compounds, it is necessary to determine which subset of spectra form a complete basis set for linear combination fitting. Some standards can be very closely approximated as a combination of others. Figures 1a and 1b show the XANES spectra of selected the Fe^{2+} and Fe^{3+} compounds, respectively. Figure 1b also depicts spectra of Fe in other oxidation states. It can be seen that many of the Fe^{2+} compounds are spectroscopically distinct (Figure 1a). In particular, Fe^{2+} phthalocyanine (Fe^{2+} –pc) shows a definite dipole-allowed $1s \rightarrow 4p$ transition at 7117 eV, which is similar to the values reported in the literature for this transition.^{25,27,40} As shown in Figure 1b, the Fe^{3+} compounds have very similar edge energy and white-line-peak height and position. The vertical line at 7120 eV emphasizes the spectroscopic differences between the 2+ and 3+ oxidation states of Fe. Because of the difficulty in interpreting the results with a large number of standards used for fitting the sample spectra, the Fe–N $_x$ standards have been grouped by category (Figure 2). Tris(2,2'-bipyridine) iron(II) hexafluorophosphate and 1,10-phenanthroline with iron(II) sulfate complex are grouped under pyridinic Fe–N $_{2+2+2}$. Fe porphine (2,3,7,8,12,13,17,18-octaethyl-21H,23H-porphine iron(III) acetate), and FeTPPS

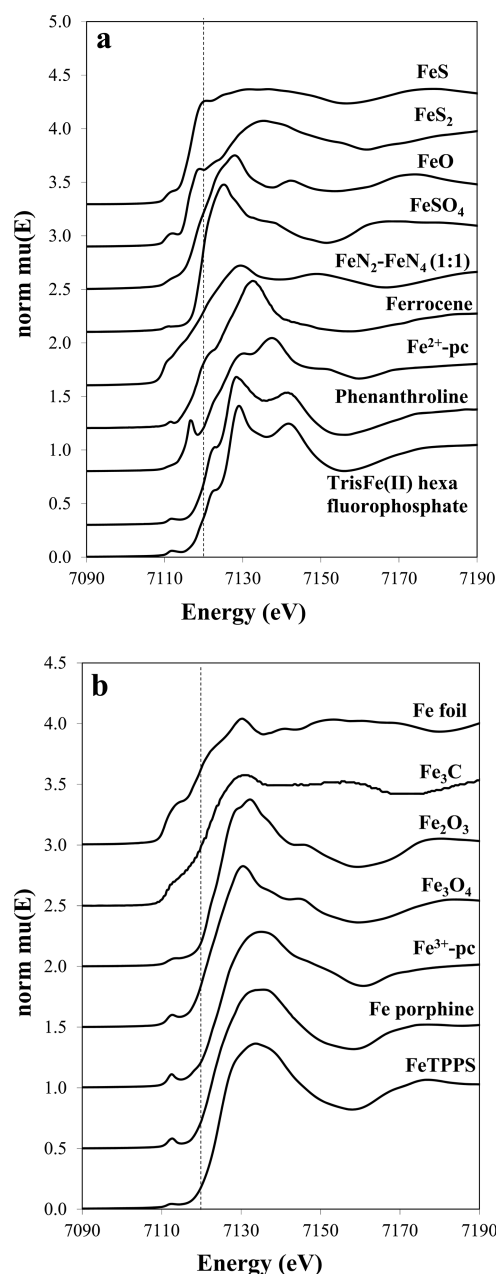


Figure 1. XANES reference spectra groupings by (a) Fe^{2+} and (b) Fe^{3+} and other Fe compounds. Fe_3C digitized from the literature.⁴¹

(5,10,15,20-tetrakis(4-sulfonatophenyl)-21*H*,23*H*-porphine iron(III) chloride) are grouped under pyrrolic $\text{Fe}-\text{N}_4$. Fe^{2+} -pc (iron(II) phthalocyanine) and Fe^{3+} -pc (iron(III) phthalocyanine-4,4',4'',4'''-tetrasulfonic acid, compound with oxygen monosodium salt) are grouped under porphyrizin $\text{Fe}-\text{N}_4$. In some cases, the contribution of each $\text{Fe}-\text{pc}$ is indicated. Ferrocene (di(cyclopentadienyl) iron) is considered an organometallic. FeS and FeS_2 are grouped under sulfides and FeO , Fe_2O_3 , and Fe_3O_4 are grouped under oxides.

We attempted to prepare iron carbide from iron nitride, but the final product was found to also contain metallic Fe and therefore was not used in the fits. Instead, the XANES spectrum of iron carbide, Fe_3C , was digitized from a literature report⁴¹ and transferred into the Athena software. Note that the spectra of the iron carbide and metallic iron have similar features (Figure 2b), in agreement with the literature.⁴²

Effect of Stages in Catalyst Synthesis. Table 1 shows the weight percent of Fe in $\text{PANI}-\text{Fe}-\text{C}$, as determined by ICP-OES after various synthesis steps and following heat treatment at different temperatures. The various steps in the catalyst synthesis include the first heat treatment (HT1), the first acid leach (AL1), the second heat treatment (HT2), and, in one case, the second acid leach (AL2). The temperatures used for both heat treatments are similar and are indicated in the table. As discussed above, these treatments are necessary and have been proven to enhance the ORR activity of this class of catalysts.^{5–8}

Before the heat treatment (BHT), the Fe loading was found to be 13 wt %. The Fe content increases up to 32.2% after the first heat treatment due to the decomposition of the polyaniline molecule,⁴³ combined with the oxidation of carbon by residual oxygen-containing species, such as ammonium peroxydisulfate. The Fe content decreases after the acid leach due to the removal of acid-soluble Fe compounds. After the second heat treatment, the Fe content increases again for the same reason as discussed above for the first heat treatment. Applying the second heat treatment after the acid leach was also reported to increase the ORR activity.^{8,44} The second acid leach did not significantly decrease the Fe loading, which indicates that the remaining Fe species are more resistant to acid treatment and/or embedded in the carbon.

Figure 3 shows the binding environment of Fe in $\text{PANI}-\text{Fe}-\text{C}$ after each synthetic step, as determined by a linear combination fitting of the XANES region of the samples to the XANES of the standards. The weight percentage was obtained by multiplying the fraction of Fe in one species by the total weight percent of Fe in the catalyst, as determined by ICP-OES analysis. Sulfide-like binding environment dominates the composition of the catalysts after heat treatments.

After the first heat treatment at 900 °C ($\text{PANI}-\text{Fe}-\text{C}_{\text{HT1}}$), the presence of iron sulfide, sulfate, oxides, metallic, and organometallic-like Fe binding environments is so dominant that other speciation cannot be estimated with sufficient accuracy. Previous XRD analysis of $\text{PANI}-\text{Fe}-\text{C}_{\text{HT1}}$ also showed the presence of sulfides and oxides.⁸ The presence of metallic Fe is not surprising as carbon can act as a reducing agent at high temperatures (“carbo-thermal reduction”). High loadings of metal precursors have been shown before to lead to metal aggregates in final catalysts.^{9,14,45,46}

In agreement with previous reports that sulfides formed during the heat treatment can be easily removed by etching,^{47,48} the first acid leach (cf. $\text{PANI}-\text{Fe}-\text{C}_{\text{HT1_AL1}}$) primarily removes iron sulfide and metallic iron, reducing the Fe content from 32.2 to 3.1 wt %. Other Fe species are also removed, indicating that the acid leach does not discriminate between various oxidation states of iron.⁴⁹ Since, at the same time, the acid leach is accompanied by an increase in ORR activity^{8,20,38} and lower hydrogen peroxide formation,⁸ one may conclude that sulfides are spectator species and their removal may actually lead to the exposure of additional active ORR sites. A similar conclusion can be made about the metallic iron.⁵⁰ Faubert et al. reported that acid leach can remove iron blocking the access of oxygen to underlying active sites.⁵¹ Acid leaching removing metallic iron agrees with an earlier observation that acid treatment increases catalyst microporosity.⁸

After the acid leach, due to the removal of major species such as sulfides, sulfates, and oxides, other species can be then detected, such as $\text{Fe}-\text{N}-\text{C}$ pyridinic-, pyrrolic-, and porphyrizin-type species. Those species become even more dominant

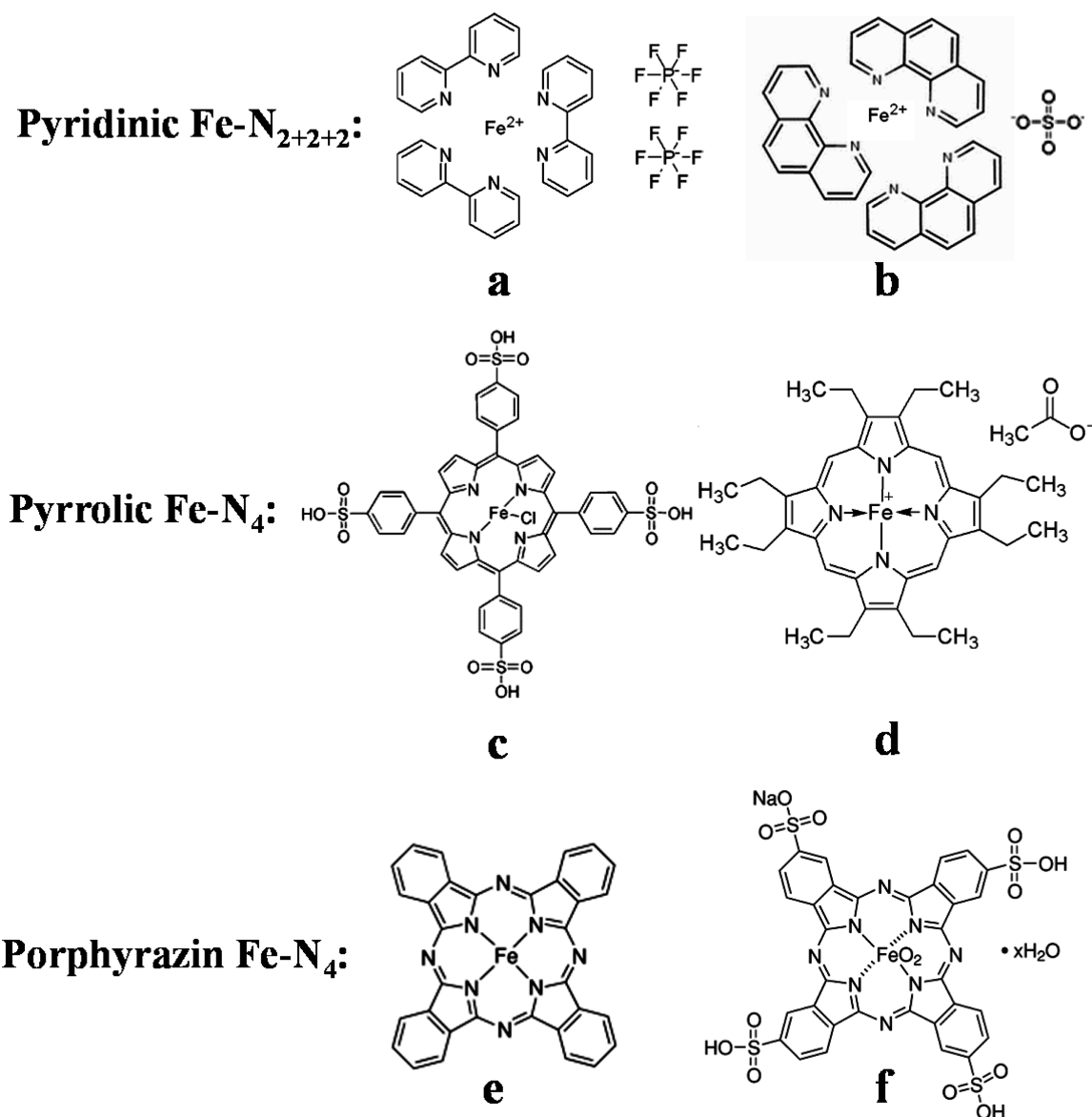


Figure 2. Grouping of Fe–N containing standards (pyridinic Fe–N₂₊₂₊₂, pyrrolic Fe–N₄, and porphyrazin Fe–N₄) used for fitting XANES spectra of Fe–PANI–C catalysts: (a) tris(2,2'-bipyridine)iron(II) hexafluorophosphate; (b) 1,10-phenanthroline iron(II) sulfate complex; (c) 5,10,15,20-tetrakis(4-sulfonatophenyl)-21H,23H-porphine iron(III) chloride (FeTPPS); (d) 2,3,7,8,12,13,17,18-octaethyl-21H,23H-porphine iron(III) acetate (porphine); (e) iron(II) phthalocyanine (Fe²⁺–pc); (f) iron(III) phthalocyanine-4,4',4'',4'''-tetrasulfonic acid, compound with oxygen monosodium salt (Fe³⁺–pc).

during the second heat treatment (PANI–Fe–C_{HT1}_AL1_HT2). In addition, the results of the linear combination fitting for samples after the acid leach and the second heat treatment indicate that the types and ratios of various iron species remain the same, only the total Fe content changes. This result is in agreement with our previous study showing the same onset potential during RDE testing for both the acid leached catalyst and the catalyst after the second heat treatment, thus indicating that the nature of the active site(s) remains unchanged throughout the different steps of catalyst preparation.⁸

Following the second heat treatment, iron carbide is detected in the catalyst sample but not metallic iron. Iron carbide is usually observed in conjunction with the heat treatment at high temperatures and in samples with high iron loading.^{45,52} Metallic iron may also be present as a result of sintering,

however, distinguishing metallic iron from iron carbide is a challenge due to their similar spectral features.

Two PANI–Fe–C samples (both after the heat treatment, the acid leach, and the second heat treatment) synthesized from different Fe content in starting precursors (3 and 10 wt %) were analyzed using Mössbauer spectroscopy. The Mössbauer parameters give information about the s-electron density at the nucleus (isomer shift), the electric field gradient on iron (quadrupole splitting), and the extent of internal magnetic fields (H_0).^{38,53} By comparison to data published in literature, one can identify the types of iron species present in the catalysts. Please note in some cases the identification of iron species was not distinct just by the Mössbauer parameters. However, knowledge of the preparation conditions combined with the characterization results from other techniques allows assignment of the most probable species responsible for the Mössbauer parameters. In Wu et al.⁸ it was shown that the

Table 1. Fe Content in PANI–Fe–C Following Different Catalyst Synthesis Steps and Heat-Treatment Temperatures^a

	wt % in catalyst
PANI–Fe–C_BHT	13.0
PANI–Fe–C_HT1_900 °C	32.2
PANI–Fe–C_HT1_AL1_900 °C	3.1
PANI–Fe–C_HT1_AL1_HT2_900 °C	9.7
PANI–Fe–C_HT1_AL1_HT2_AL2_900 °C	7.4
PANI–Fe–C_HT1_AL_HT2_600 °C	2.1
PANI–Fe–C_HT1_AL_HT2_800 °C	2.6
PANI–Fe–C_HT1_AL_HT2_850 °C	3.2
PANI–Fe–C_HT1_AL_HT2_950 °C	10.0
PANI–Fe–C_HT1_AL_HT2_1000 °C	8.4
S-free-PANI–Fe–C_HT1_900 °C	2.7
S-free-PANI–Fe–C_HT1_AL_HT2_900 °C	1.5

^aBHT: before heat treatment; HT1: first heat treatment; AL1: first acid leach; HT2: second heat treatment; AL2: second acid leach.

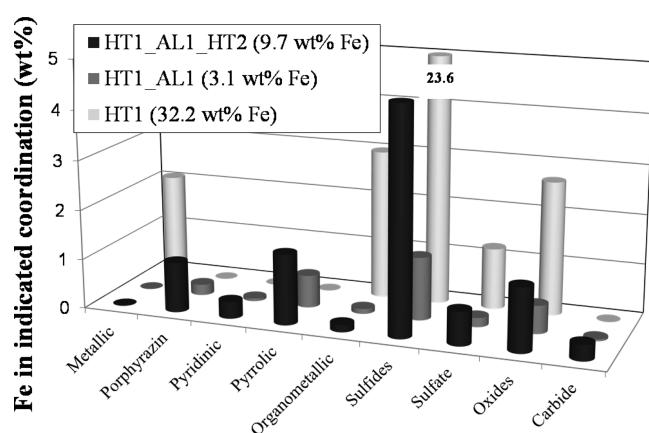


Figure 3. Weight percentage of Fe species in PANI–Fe–C catalysts after different steps in the synthetic procedure. HT1: first heat treatment; AL1: first acid leach; HT2: second heat treatment. Total iron content is given in parentheses.

obtained ORR activity depends on the initial (and thus final) iron contents. The kinetic current density increased up to a content of 3 wt %; above this value it stayed constant. Therefore, the comparison of two catalysts with different iron contents (but similar activity) is helpful for elucidating the effect of Fe speciation on ORR activity.

The Mössbauer spectra of both catalysts were fitted with singlet, doublet, or sextet lines. Figure 4 shows a spectrum for the catalyst with a final Fe loading of 3 wt %. The assignments of the singlet, doublets, and sextets are given in Table 2, with corresponding literature listed in support of the assignments. Table 2 also gives the Mössbauer parameters associated with both catalysts. It can be seen that the iron species formed as a result of the heat treatment are similar for both catalysts, but their relative distributions are different. The two samples contain superparamagnetic α -iron (singlet), low-spin Fe^{2+}N_4 centers, and/or superparamagnetic FeO (doublet D1), a 3-fold coordinated high spin $\text{CFe}^{2+}\text{N}_2$ and/or $[\text{FeN}_4]^{2-}$ (doublet D2), a ferrous high-spin center, possibly Fe–N_4 and/or FeCl_2 (doublet D3), Fe_3S_4 (sextet 1), nonstoichiometric Fe_xN (sextet 2), and Fe_3C (sextet 3). As expected, the sample with a lower Fe content in the precursor (Cat1) has a much smaller overall magnetic contribution compared to Cat2.

Though the catalysts were heat-treated in a reducing atmosphere, which would favor the assignment of the doublet D1 to Fe–N_4 instead of superparamagnetic FeO, the presence of FeO resulting from post-heat-treatment exposure to air cannot be ruled out. For the doublet D2, the presence of both types of iron species, $\text{CFe}^{2+}\text{N}_2$ and $[\text{FeN}_4]^{2-}$, is feasible given the preparation method. With respect to doublet D3, the large quadrupole splitting reflects the large electric field gradient at the iron nucleus. The doublet D3 can be attributed to a 5- or 6-fold coordinated Fe–N_4 center with axial ligands other than nitrogen or to residual FeCl_2 . Both samples contain sulfides (Sext1), but a much larger contribution is seen for the “standard catalyst” (Cat2). Since a larger amount of iron precursor was used in the synthesis of Cat2 than Cat1, the

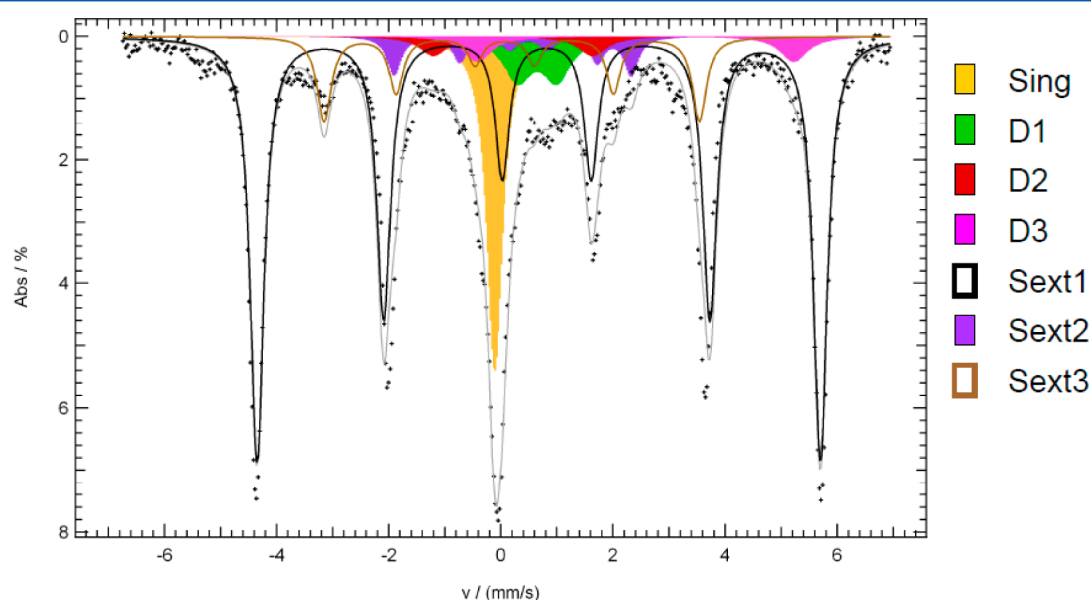


Figure 4. Mössbauer spectrum of PANI–Fe–C_HT1_AL1_HT2 (after the first heat treatment at 900 °C, acid leach, and the second heat treatment at 900 °C) measured at room temperature. Final catalyst loading is 3 wt % Fe.

Table 2. Mössbauer Parameters for PANI–Fe–C Catalysts with 3 wt % Fe (Cat1) and 10 wt % Fe (Cat2) Measured at Room Temperature; Assignment of the Singlet, Doublets and Sextets Observed for the PANI–Fe–C Catalysts and Corresponding References

	isomer shift δ (mm/s)		quadrupole splitting ΔE (mm/s)		half-width hyperfine field H_0 (T)		fwhm (mm/s)	rel area A (%)		assignt
	Cat1	Cat2	Cat1	Cat2	Cat1	Cat2		Cat1/2	Cat1	
singlet	−0.07	−0.09					0.34(f)	5.1	12.3	superparam iron (no interaction of Fe particles) [53]
D1	0.35	0.26	1.03	1.03			0.6(f)	16.0	5.8	Fe−N ₄ (3d ⁶ , LS) and/or superparam FeO [13, 37]
D2	0.61	0.43	1.52	1.37			0.6(f)	15.5	3.8	CFeN ₂ and/or [FeN ₄] ^{2−} [54, 55]
D3	1.06	1.01	3.99	4.03			0.6(f)	7.0	2.5	Fe ²⁺ , HS maybe Fe−N ₄ and/or iron halide [56]
Sext1	0.71	0.68	−0.12	−0.15	30.6	30.3	0.3(f)	19.5	61.5	Fe ₃ S ₄ (Greigit) [57]
Sext2	0.44	0.44	−0.17	−0.22	11.9	11.7	0.3(f)	11.3	5.9	nonstoichiometric Fe _x N or other phase [58, 59]
Sext3	0.16	0.04	0.05	0.19	20.8	20.8	0.3(f)	25.6	8.2	Fe ₃ C [53, 60]

amount of FeS_x (Sext1) formed in the reaction between iron and APS is larger in Cat2 than in Cat1.

Both catalysts reveal significant contributions from iron carbide and/or α -Fe (see singlet and Sext3). If the particle size of iron and/or iron carbide is too small (<20 nm), the magnetic interaction is too weak to generate a sextet line within a Mössbauer spectrum. In this case one will observe a singlet assigned to superparamagnetic α -iron. With respect to the investigated catalysts, it seems that the larger content of sulfur in Cat2 hinders the formation of larger Fe₃C particles assigned to Sext3; however, the fraction of the Singlet is larger. In previous studies, the addition of sulfur has been found to hinder the formation of iron carbide.^{47,48} As thermodynamic calculations have shown, however, this is only possible for heat treatment temperatures ≤ 800 °C, even when the sulfur content is increased.⁶¹ Since the heat treatment temperature exceeded 800 °C in this study, the formation of iron carbide was not completely suppressed by the presence of sulfur. With respect to the different contents of the singlet vs Sext3, one might conclude that the higher mass fraction of sulfur in Cat2 hinders both the graphitization⁶² and the formation of larger iron carbide agglomerates.⁴⁸ Therefore, Cat2 contains the smaller fraction of Sext3 but a higher content of the singlet iron species.

The high initial iron sulfate content appears to suppress the interaction of iron with the nitrogen atoms from polyaniline needed to form Fe–N₄ centers. As a consequence, the relative content of Fe–N₄ to total Fe is smaller for Cat2 compared to Cat1. Cat2 contains a large fraction of Fe₃S₄ rather than Fe–N₄. It might be assumed that, from a thermodynamic point of view, the iron sulfate is reduced to Fe₃S₄ and that this species exhibits higher temperature stability under heat treatment conditions than Fe–N₄ centers.

As mentioned above, in Wu et al.⁸ the catalysts with 3 wt % Fe and 10 wt % Fe exhibited similar RDE performance. The absolute content of Fe–N₄ centers, as calculated using the D1 Mössbauer lines, is similar for these two catalysts. This may be a further indication that these types of sites contribute to ORR activity.

Effect of Heat-Treatment Temperature. The Fe content after the acid leach and the second heat treatment is shown in Table 1 for PANI–Fe–C_HT1_AL1_HT2 as a function of the heat-treatment temperature between 600 and 1000 °C. The observed decrease in the Fe content relative to the initial Fe content is larger for samples heat-treated at lower temperatures, between 600 and 850 °C. This implies that inorganic Fe compounds formed at higher heat-treatment temperatures have

better acid stability compared to the Fe-containing species formed at lower temperatures. Once the heat-treatment temperature exceeds 900 °C, the final Fe content stabilizes between 8 and 10 wt %.

Figure 5 shows the effect of the heat-treatment temperature on the XRD patterns for PANI–Fe–C_HT1_AL1_HT2. For

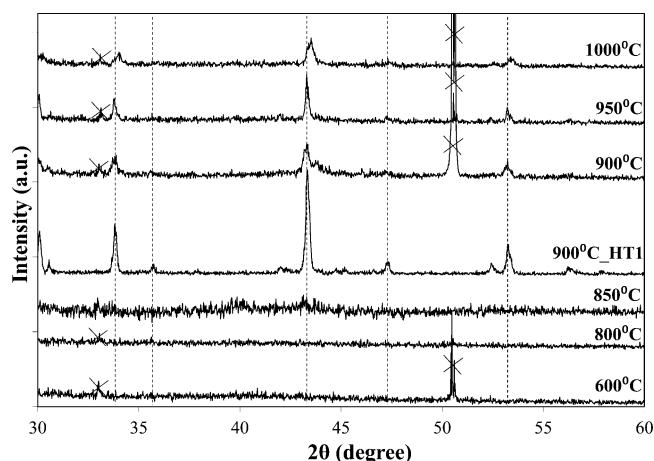


Figure 5. Effect of the heat-treatment temperature on XRD patterns of PANI–Fe–C_HT1_AL1_HT1 catalysts (after the first heat treatment, acid leach, and second heat treatment at the temperature indicated). Comparison with PANI–Fe–C_HT1 (after the first heat treatment at 900 °C). Crossed peaks arise from the sample holder.

all samples the temperatures of the two heat treatments, HT1 and HT2, were the same. There are no resolvable XRD peaks for the samples prepared at 600, 800, and 850 °C. Above 850 °C, the FeS peaks ($2\theta = 31.9^\circ, 33.7^\circ, 35.6^\circ, 43.3^\circ, 47.2^\circ$, and 53.2°) can be seen, which shift toward higher 2θ with an increase in the heat-treatment temperature, indicating the formation of Fe_(1-x)S with a gradually increasing S-to-Fe ratio. A comparison of the diffraction patterns for PANI–Fe–C_HT1 (900 °C_HT1) and PANI–Fe–C_HT1_AL1_HT2 (900 °C) reveals that the acid leach removes a substantial amount of Fe_(1-x)S.

Figure 6 shows the composition of Fe compounds in weight percent for PANI–Fe–C_HT1_AL2_HT2 (heat-treated, acid-leached, and heat-treated again catalyst), determined by XANES linear combination fitting, as a function of the heat-treatment temperature. The ORR activity, the BET surface area, and the microporous surface area as a function of the heat-treatment temperature are also shown in Figure 6a. All three plots in that figure follow the same trend. The XANES results

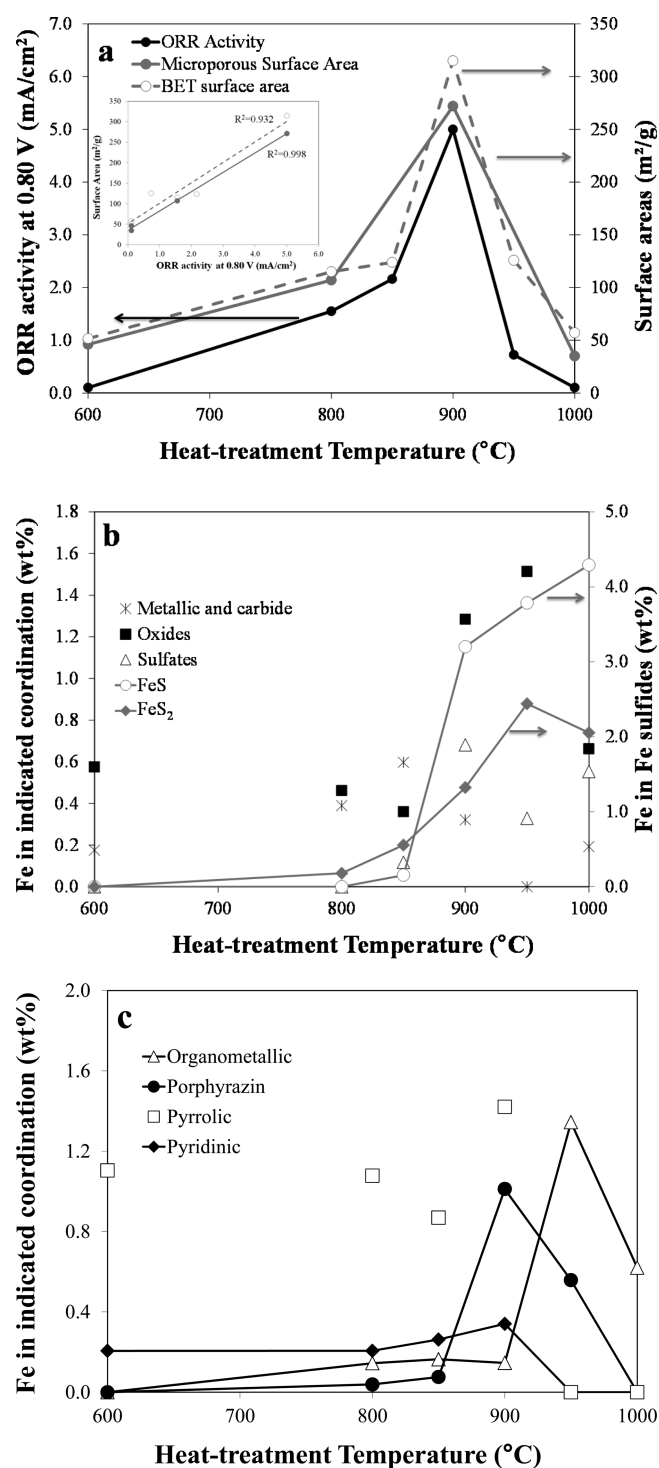


Figure 6. Effect of the heat-treatment temperature during the synthesis of PANI-Fe-C on (a) ORR activity, BET and microporous surface areas; (b, c) weight percentage of Fe species. Data recorded after the heat treatment, acid leach, and the second heat treatment at the temperature indicated.

in Figure 6b show that the amount of iron sulfides increases drastically following heat treatment at temperatures above 850 °C. These results also show that FeS₂ dominates over FeS in the samples heat-treated at 800 and 850 °C, while the opposite is observed with samples treated at 900 and 1000 °C. The iron oxide content is the highest following heat treatments at 900 and 950 °C. The amount of metallic Fe and Fe carbide, species

reported to be inactive for the ORR,^{45,52,63} is low, with a maximum content obtained after the heat treatment at 850 °C. The sample heat-treated at 900 °C contains the largest amount of Fe-porphyrizin-type coordination, as well as the largest amount of pyrrolic and pyridinic nitrogen species. However, the effect of the heat-treatment temperature on the formation of these two species is less than on that of porphyrizin-type species (Figure 6c). While the amount of porphyrizin species decreases significantly once the heat-treatment temperature exceeds 900 °C, a significant fraction of these species can be found in the sample heat-treated at 950 °C. Pyrrolic and pyridinic species are nearly absent in the catalyst heat-treated at 950 °C.

Noteworthy, the maximum ORR activity and selectivity (i.e., the minimum hydrogen peroxide yield), as determined in the RDE experiments, are both reached with the PANI-Fe-C catalyst heat-treated at 900 °C.^{5,7,8} The catalyst heat-treated at 900 °C also has the highest BET surface area and the highest microporous surface area. The microporous surface area of PANI-Fe-C is lower than that of the carbon support (650 m²/g⁸); however, it is the microporosity generated during the heat treatment that is often tied to the ORR activity of nonprecious metal catalysts.^{64–66}

There is a strong linear correlation between the ORR activity and both the BET area and microporous surface area, as shown by the R^2 values of 0.93 and 0.99, respectively (inset in Figure 6a). The ORR activity is also strongly correlated with the presence of Fe-N_x species ($R^2 = 0.76$), especially with the Fe-N₄ porphyrizin ($R^2 = 0.60$) and the sum of Fe-N₄ porphyrizin and pyridinic Fe-N₂₊₂₊₂ ($R^2 = 0.80$). Much weaker correlation of the ORR activity with the content of pyrrolic Fe-N₄ species is observed ($R^2 = 0.41$). There is no correlation between ORR activity and iron oxides and sulfides content ($R^2 \leq 0.1$).

According to the selected studies published to date, the optimum heat-treatment temperature for the formation of Me-N₄ centers in ORR-active catalysts is between 500 and 800 °C,¹⁹ and the contribution from Fe-N₄ centers is decreased after heat treatment at higher temperatures.^{14,15,38,67} However, other reports indicate that high ORR activity can be generated by the heat treatment at high temperatures.^{9,16,68} As an explanation for this discrepancy it was discussed that electronic changes in the Fe-N₄ centers enables higher turnover frequencies.^{12,38} Therefore, even though the overall number of active sites is smaller, higher current densities can be obtained. This is the case for the PANI-Fe-C catalyst in this study, for which the heat treatment at a temperature of 900 °C yields the highest ORR activity, attributed by some to the presence of oxidized iron and pyridinic nitrogen functionalities (rather than Fe-N₄ centers).⁴⁵ The heat treatment temperature of 900 °C was also found to lead to the most active and stable catalysts in the studies by Dodelet and co-workers.^{18,20,51}

Notwithstanding a possible role of Fe-N_x centers in assuring high ORR activity, FeO_x is also believed to be involved in inducing ORR activity but presumed to be less active than either Fe-N₂₊₂/C or Fe-N₄/C.⁶⁸ However, our XANES studies show a very weak correlation between the ORR activity and the iron oxide content in PANI-Fe-C catalysts ($R^2 = 0.09$).

In this study, both pyrrolic Fe-N₄ and pyridinic Fe-N₂₊₂₊₂ are found in the catalysts following the heat treatment up to 900 °C and porphyrizin Fe-N₄ after heat treatment between 800 and 950 °C. Note that the pyridinic Fe-N might also be assigned to Fe-N₂ and Fe-N₂₊₂. The fact that Fe-N₄

functionalities are still present at high temperatures may be due to the use of sulfur in this study, which, by lowering the amount of carbide formed, prevents the destruction of Fe–N₄ centers.⁶⁸

The N and Fe speciation in the PANI–Fe–C catalysts was analyzed using XPS. Figure 7 depicts a high-resolution N 1s

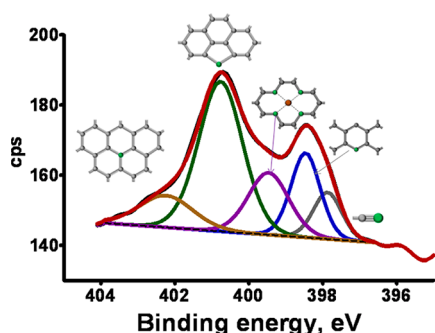


Figure 7. N 1s high-resolution XPS spectrum of the PANI–Fe–C_HT1_AL1_HT2 (after the heat treatment at 900 °C, acid leach, and the second heat treatment at 900 °C).

spectrum recorded with the PANI–Fe–C_HT1_AL1_HT2_900 °C catalyst sample. Table 3 shows N and Fe speciation, given in atomic %, for all catalyst samples following the first heat treatment, the acid leach, and the second heat treatment. Five peaks representing N functionalities are detected: a cyano group N at 398.1 eV, pyridinic N at 398.6 eV, N coordinated to Fe (N–Fe) at 399.6 eV, pyrrolic N at 400.9 eV, and a combination of quaternary and graphitic N (Ngr) at 402 eV. The absolute amount of N increases slightly after the catalyst is heated-treated at 400 °C with an increase in the pyridinic and N–Fe species and a decrease in the quaternary and graphitic nitrogen. Already, at temperatures >400 °C the nitrogen content decreases. However, significant decreases of the overall nitrogen and the N–Fe contents are observed for temperatures exceeding 800 °C. As discussed above, sulfur addition suppresses carbide formation and graphitization only up to 800 °C.⁴⁸ Changes in the atomic % of individual N species present (data not shown) indicate that with increasing heat treatment temperature the amount of pyrrolic and graphitic/quaternary nitrogens increases. The change of the relative content of the different nitrogen species is in accord with Pels et al.⁶⁹ In that work the authors discussed that the high temperature induces a condensation reaction of pyrrolic and pyridinic to quaternary nitrogen. The atomic % of Fe–N (Fe 2p) and N–Fe (N 1s) differ as a result of different sensitivities,⁷⁰ covering of particles by carbon pyropolymer,

photoionization cross sections, attenuation length, and sampling depth.

With increasing heat-treatment temperature, carbon loss and rearrangement of the structure cause an increase in Fe concentration in the near-surface region. The XPS analysis shows that the amount of Fe–N reaches a maximum following heat treatment at 900 °C, as was also observed in the XANES results (Figure 6c). The Fe₃O₄/FeO content reaches a maximum after the treatment at 950 °C, also in agreement with the XANES data (Figure 6b). The maximum FeS content was found in the samples heat-treated at 950–1000 °C. FeS is more abundant than FeS₂, in agreement with the XANES results (Figure 6b).

The correlation between the ORR activity and the atomic % of nitrogen and Fe species in PANI–Fe–C catalysts is shown in Figure 8. The contents of pyridinic N and pyrrolic N follow

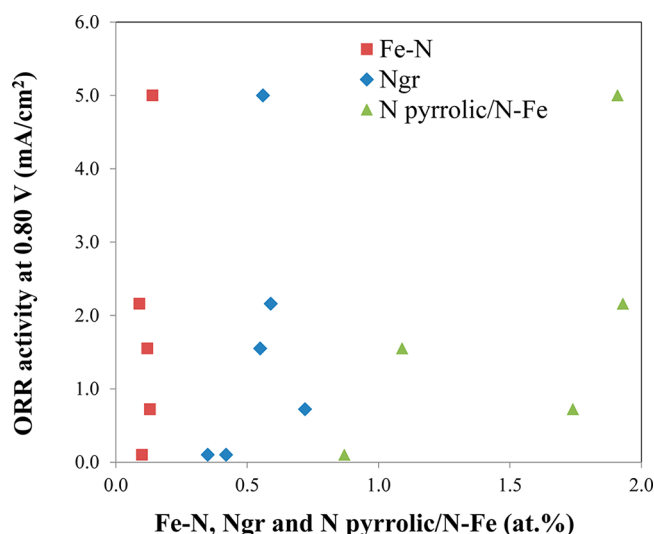


Figure 8. Atomic % of Fe–N, Ngr (quaternary and graphitic N), N pyrrolic/N–Fe versus ORR activity of PANI–Fe–C catalysts heat-treated at various temperatures. ORR activity determined in RDE experiments at 0.80 V vs RHE. All tests performed with catalysts after the first heat treatment, acid leach, and the second heat treatment.

very weak linear inverse relationship with the ORR activity ($R^2 < 0.1$), not shown here. Ngr (quaternary and graphitic N) is the only nitrogen functionality that exhibits a weak linear relationship with the ORR activity ($R^2 = 0.11$). The Fe–N content, determined from Fe 2p spectra also shows a weak linear relationship with ORR activity ($R^2 = 0.32$); however, the exclusion of data corresponding to the catalyst obtained after

Table 3. N and Fe Speciation (at. %) from XPS Analysis for PANI–Fe–C before the Heat Treatment (BHT) after the Heat Treatment, the Acid Leach, and the Second Heat Treatment at Indicated Temperatures (°C)

heat-treatment temp (°C)	cyano 398.1 eV	N pyridinic 398.6 eV	N–Fe 399.6 eV	N pyrrolic 400.9 eV	Ngr 402.0 eV	total N (at. %)	FeS ₂ 708.0 eV	Fe–N 709.2 eV	FeO/Fe ₃ O ₄ 710.3 eV	Fe–S/Fe ₃ O ₃ 711.6 eV	FeSO ₄ 712.9 eV	total Fe (at. %)
BHT	0.02	0.33	2.03	1.59	3.81	7.8	0.04	0.77	1.32	1.89	1.21	5.2
400	0.16	3.13	3.54	2.37	0.47	9.7	0.04	0.01	0.04	0.04	0.06	0.2
600	0.60	1.77	1.84	1.60	0.35	6.2	0.02	0.10	0.03	0.06	0.06	0.3
800	1.31	0.88	1.43	1.57	0.55	5.7	0.02	0.12	0.07	0.10	0.15	0.5
850	0.50	0.83	0.63	1.23	0.59	3.8	0.07	0.09	0.08	0.08	0.11	0.4
900	0.53	0.52	0.71	1.37	0.56	3.7	0.06	0.14	0.12	0.10	0.07	0.5
950	0.23	0.40	0.61	1.06	0.72	3.0	0.04	0.13	0.16	0.20	0.16	0.7
1000	0.24	0.49	0.43	1.31	0.42	2.9	0.15	0.10	0.14	0.20	0.13	0.7

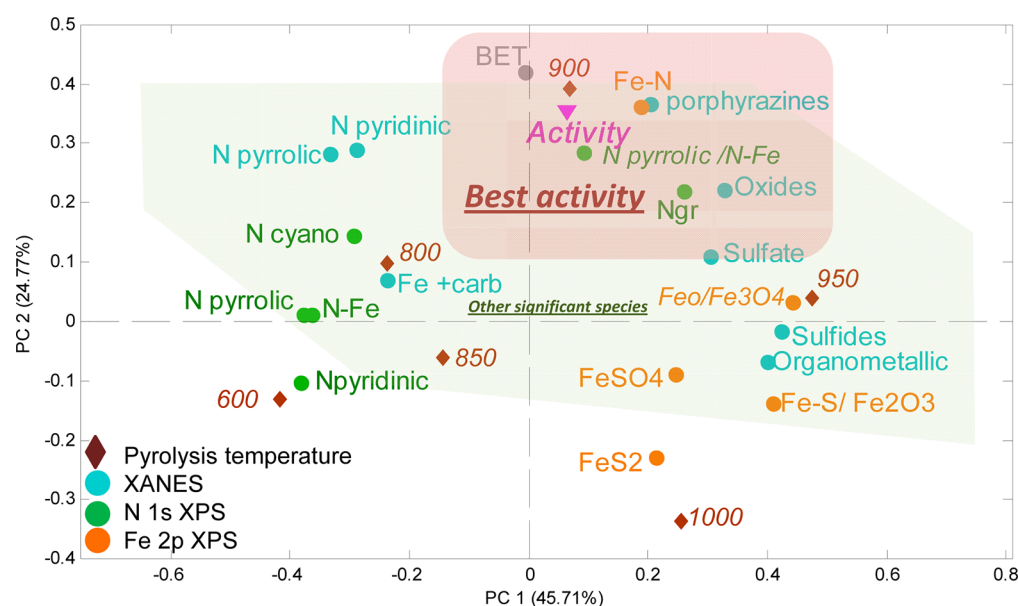


Figure 9. Correlation between XANES, XPS, and BET data and ORR activity for PANI–Fe–C using principal component analysis. All catalysts after heat treatment, acid leach, and a second heat treatment.

heat treatment at 850 °C (which showed an anomalously low Fe–N content) improves the correlation to $R^2 = 0.65$. The ratio of N pyrrolic to N–Fe species shows a mild linear relationship with the ORR activity ($R^2 = 0.40$). This indicates that the total amount of nitrogen species may not be as relevant to the ORR activity as the relative distribution of N species with respect to each other. The XPS data indicate that ORR activity increases with increasing percentage of Fe–N and with increasing number of pyrrolic nitrogens with respect to N–Fe species.⁷¹

Even though some trends are clear from the data shown in Figure 8, Table 3 (XPS), and Figure 6 (XANES), multivariate statistical methods of data analysis highlight similarities and differences between samples and point to correlations between variables that might not be obvious otherwise. The XANES linear fits and XPS speciation were combined with electrochemical activity and surface area data into a single data matrix, and principal component analysis (PCA) was applied to these data. While the BET surface area was used instead of the microporous area (only the BET data were available at all heat treatment temperatures) the trends turned out to be similar for both the BET and microporous area data sets (Figure 6a). The function of PCA is to find samples which are similar or different and to facilitate visualization of the variables responsible for the similarities/differences. Biplots are used herein to simplify association of variables from multiple techniques for various samples. Correlated parameters and samples are located in the same quadrant on a biplot. Figure 9 shows a PCA biplot displaying two first principal components' loadings (showing the relationship between variables) and scores (showing the relationship between samples). Principal component 1 captures 48% of the data variance and separates high-temperature samples (contributing positively into PC1) from low-temperature samples (contributing negatively into PC1). Principal component 2 captures 22% of the data variance and separates samples by activity, i.e., better-performing samples contributing positively into PC2 and worse-performing samples contributing negatively into PC2. The quadrant into which both PCs contribute positively contains the PANI–Fe–C samples heat-treated at 900 and 950 °C, the samples with the highest ORR

activity, and the BET surface area. The sample heat-treated at 900 °C has a high contribution from a cluster of variables closely located to it within this quadrant. The ORR activity is correlated with Ngr, Fe–N, and the ratio between N pyrrolic/N–Fe, as determined by XPS (plotted in Figure 8), and with porphyrizin, as determined by XANES. The PANI–Fe–C sample heat-treated at 950 °C has a higher content of sulfates, organometallics, and sulfides, from XANES analysis, and S–Fe-containing species, as determined by XPS. The PANI–Fe–C sample heat-treated at 800 °C, which contributes positively into PC2, also has high activity and a higher presence of pyrrolic and pyridinic species, as determined by both XANES and XPS. A very good correlation between the XANES and XPS-determined speciation is observed. It is important to remember that the XPS signal arises from material within 10 nm of the surface, whereas XANES is a bulk spectroscopic technique. The presence of pyridinic and pyrrolic nitrogens in the samples heat-treated at low temperatures is more prevalent in the XPS data than in the XANES data, which might indicate that these species either exist or have been formed at the surface at low temperatures and then penetrated into bulk with increasing heat-treatment temperature.

Effect of Synthesis Procedure: Sulfur-Free Oxidant. In one of the catalyst synthesis methods used, the ammonium peroxydisulfate was replaced by hydrogen peroxide as a sulfur-free oxidant. The goal was to eliminate the formation of iron sulfides during the heat treatment instead of removing iron sulfides by the acid leach, which is not fully effective. This also allowed for the assessment whether sulfur-containing species contribute to the ORR or not. As shown in the present and previous studies, the removal of iron sulfides by the acid leach results in an increase in ORR activity.^{8,72} However, without sulfur present, iron carbides are known to be formed and Fe–N₄ species destroyed.⁴⁸ Our present Mössbauer study indicates that a large amount of sulfur may also impede the formation of Fe–N₄ centers. Thus, there must be an optimum Fe/S ratio in which the maximum Fe–N₄ centers can be reached. Similar conclusions were made by Herrmann, who investigated the changes in RDE performance of (Co,Fe)–N–C catalysts

prepared by the oxalate-supported pyrolysis of CoTMPP.⁷³ In that work, up to a specific S content in the precursor mixture the kinetic current density was increased. Above this optimal content, however, the kinetic current density decreased. Furthermore, elemental analysis of the final catalysts exhibited a drastic increase in the sulfur content above this optimum.

Figure 10 shows the wt % of Fe for the S-free PANI–Fe–C catalyst after the first heat treatment at 900 °C (HT1) and after

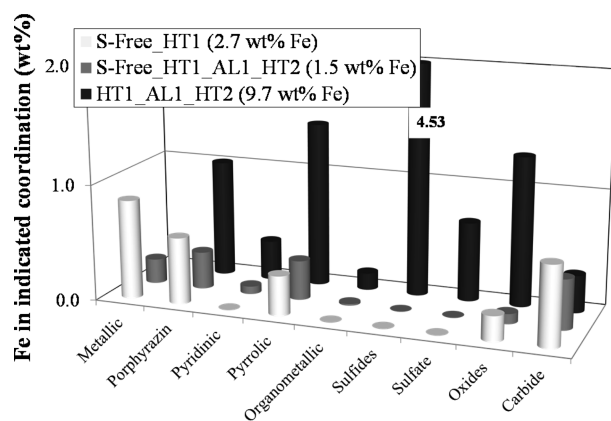


Figure 10. Weight percentage of Fe species following different synthesis steps of S-containing and S-free PANI–Fe–C. HT1: the first heat treatment at 900 °C; AL1: the acid leach; HT2: the second heat treatment at 900 °C. Total iron content given in parentheses.

the acid leach, and the second heat treatment (HT1_AL1_HT2) in comparison to the S-containing PANI–Fe–C catalyst that had undergone the same treatment. The total amount of Fe in the S-free sample, as determined by ICP-OES, is 2.7 wt % after the first heat treatment and 1.5 wt % after the first heat treatment, acid leach, and second heat treatment. These values are much lower than those found for the S-containing sample (32.2 wt % for the PANI–Fe–C_HT1 and 9.7 wt % for the PANI–Fe–C_HT1_AL1_HT2). In the S-free samples, the amount of iron carbide is higher than in the S-containing PANI–Fe–C sample. Furthermore, the amount of the porphyrizin, pyridinic, and pyrrolic nitrogen functionalities is smaller than in the S-containing sample. This is in agreement with the literature claiming that the absence of sulfur results in a lower total amount of N, which limits the number of Fe–N₄ centers.⁴⁸ Thus, there is an indirect advantage of having sulfur-based precursors in the catalyst synthesis, which in this case was the ammonium peroxydisulfate used as an oxidant in the polymerization of aniline.

Figure 11 shows RDE polarization plots recorded with the standard S-containing PANI–Fe–C catalyst and the S-free PANI–Fe–C catalyst. On the basis of the half-wave potential of the RDE experiments ($E_{1/2}$), the S-containing PANI–Fe–C is more ORR-active than the S-free PANI–Fe–C ($\Delta E_{1/2} = 0.026$ V). PANI–Fe–C also contains a higher concentration of Fe–N₂ and Fe–N₄ centers combined than the S-free PANI–Fe–C. Since the iron sulfides are eliminated and the iron metal content is decreased while ORR activity is maintained, those iron species are not likely to play a key role in the formation of the ORR active sites.

An important issue is the durability of the Fe-based catalysts. Fortunately, the PANI–Fe–C catalyst presented here has higher durability than most Fe-type catalysts, as previously published in Figure 5 in Jaouen et al.⁷⁴ The activity data that

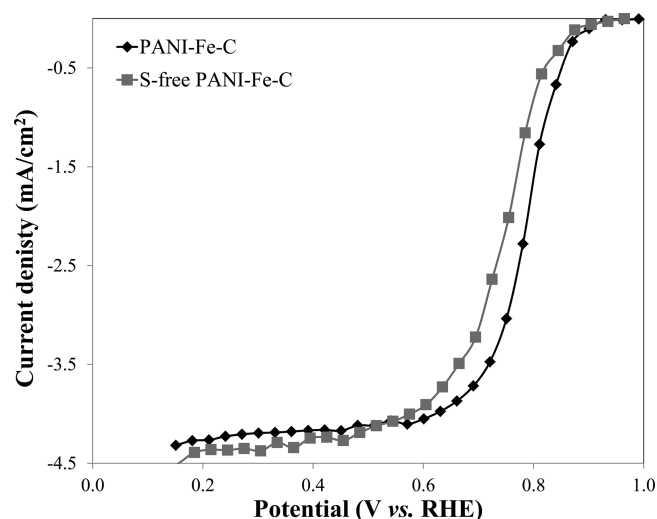


Figure 11. ORR activity as measured by RDE of PANI–Fe–C and S-free PANI–Fe–C catalysts first heat-treated at 900 °C and then subjected to the acid leach and the second heat treatment at 900 °C. The ORR steady-state polarization curves were recorded in oxygen-saturated 0.5 M H₂SO₄ electrolyte with a potential step of 0.03 V and a holding time at each potential of 30 s. After 30 s, when the background capacitive current had passed, a steady-state value of the Faradaic current was measured.

are presented here can therefore be considered representative of the initial state of the catalyst, and the relationship between initial composition and the activity values is clearer than for some other Fe-based catalysts. We have performed an extensive and detailed X-ray study comparing the loss of different forms of Fe and the loss in activity at 0.40 and 0.60 V for the optimized catalysts in fuel cell tests. In brief, the results confirm the longevity and importance of Fe–N_x species. Thus, no contradiction was found with the results presented here when the durability information is also considered, but this work is substantial enough to be presented separately in a forthcoming publication.⁷⁵

CONCLUSIONS

A PANI–Fe–C non-precious metal ORR catalyst has been studied at different stages of the synthesis, following the heat treatment at various temperatures, and using two types of oxidant in the polymerization of aniline. XANES linear combination fitting was used to determine the speciation of Fe using 16 iron standards. The catalyst samples were also characterized by XPS, Mössbauer spectroscopy, X-ray diffraction, BET surface area and microporous surface area, and ICP-OES. It was found that:

(1) Heat treatment at temperatures exceeding 850 °C followed by an acid leach at 80 °C yields catalysts with Fe content of 8–10 wt %. The use of lower heat-treatment temperatures results in a lower Fe content due to either a higher solubility in acid of the Fe species formed at low temperatures or protection from the acid by the carbon coatings around the Fe species after heat treatment at higher temperatures. If ammonium peroxydisulfate is used in the aniline polymerization, a significant fraction of Fe in catalysts formed at temperatures exceeding 850 °C is present in the form of iron sulfides (FeS_x).

(2) The highest ORR activity is shown by a PANI–Fe–C catalyst obtained in a process involving the heat treatment 900

°C, acid leach, and a second heat treatment at 900 °C. This process results in the highest sample microporosity and the highest Fe–N₄ (porphyrizin) content (as determined by XANES).

(3) Principal component analysis using XANES linear fits, XPS speciation, electrochemical activity, and surface area data reveals very good correlation between the ORR activity and the Fe and N speciation. The ORR activity correlates well with the total of quaternary and graphitic N, Fe–N, and the ratio of pyrrolic N to N–Fe, as determined by XPS. The activity also correlates with the BET surface area, the microporous surface area, and with Fe–N content, especially that of Fe in the porphyrizin and pyridinic coordination, as determined by XANES. A good correlation with the ratio of pyrrolic N to N–Fe indicates that the total amount of nitrogen species may not be as important for inducing the ORR activity as the relative distribution of the N species with respect to each other.

(4) The formation of FeS_x in the catalyst can be eliminated by using a sulfur-free oxidant in the aniline polymerization. However, as shown in this work, such modifications to the PANI–Fe–C catalyst synthesis results in the formation of more iron carbide, fewer Fe–N₄ centers, and lower ORR activity. The Mössbauer study of samples with varying amounts of FeS_x indicates that, to a certain extent, sulfur is beneficial to the formation of Fe–N₄ centers.

AUTHOR INFORMATION

Corresponding Author

*Phone 1-630-252-2566; e-mail ferrandon@anl.gov.

Notes

The authors declare no competing financial interest.

ACKNOWLEDGMENTS

The authors thank Analytical Chemistry Laboratory at Argonne for the elemental analysis. This work was supported by the U.S. Department of Energy, Office of Energy Efficiency and Renewable Energy, Fuel Cell Technologies Program. Argonne National Laboratory is managed for the U.S. Department of Energy by the University of Chicago Argonne, LLC, under Contract DE-AC-02-06CH11357. The use of Advanced Photon Source was supported by the U.S. Department of Energy, Office of Science, and Office of Basic Energy Sciences. Work performed at the Materials Research Collaborative Access Team (MRCAT) beamline was supported, in part, by funding from the U.S. Department of Energy under Grant DE-FG02-04ER46106.

REFERENCES

- (1) Wang, B. *J. Power Sources* **2005**, *152*, 1–15.
- (2) Jasinski, R. *J. Nature* **1964**, *201*, 1212–1213.
- (3) Jasinski, R. *J. Electrochem. Soc.* **1965**, *112*, 526–528.
- (4) Wu, G.; Chen, Z.; Artyushkova, K.; Garzon, F. H.; Zelenay, P. *ECS Trans.* **2008**, *16* (2), 159–170.
- (5) Wu, G.; Artyushkova, K.; Ferrandon, M.; Kropf, J.; Myers, D.; Zelenay, P. *ECS Trans.* **2009**, *25* (1), 1299–1311.
- (6) Wu, G.; Nelson, M. A.; Mack, N. H.; Ma, S.; Sekhar, P.; Garzon, F. H.; Zelenay, P. *Chem. Commun.* **2010**, *46* (40), 7489–7491.
- (7) Wu, G.; More, K. L.; Johnston, C. M.; Zelenay, P. *Science* **2011**, *332*, 443–447.
- (8) Wu, G.; Johnston, C. M.; Mack, N. H.; Artyushkova, K.; Ferrandon, M.; Nelson, M.; Lezama-Pacheco, J. S.; Conradson, S. D.; More, K. L.; Myers, D. J.; Zelenay, P. *J. Mater. Chem.* **2011**, *21*, 11392–11405.

- (9) Lefèvre, M.; Dodelet, J. P. *J. Phys. Chem. B* **2000**, *104* (47), 11238–11247.
- (10) Bron, M.; Radnik, J.; Fieber-Erdmann, M.; Bogdanoff, P.; Fiechter, S. *J. Electroanal. Chem.* **2002**, *535*, 113–119.
- (11) Bouwkamp-Wijnoltz, A. L.; Visscher, W.; van Veen, J. A. R.; Boellaard, E.; van der Kraan, A. M.; Tang, S. C. *J. Phys. Chem. B* **2002**, *106*, 12993–13001.
- (12) van Veen, J. A. R.; Colijn, H. A.; van Baar, J. F. *Electrochim. Acta* **1988**, *33* (6), 801–804.
- (13) Koslowski, U. I.; Abs-Wurmbach, I.; Fiechter, S.; Bogdanoff, P. *J. Phys. Chem. C* **2008**, *112*, 15356–15366.
- (14) Bae, I. T.; Tryk, D. A.; Scherson, D. A. *J. Phys. Chem. B* **1998**, *102* (21), 4114–4117.
- (15) Lefèvre, M.; Dodelet, J. P.; Bertrand, P. *J. Phys. Chem. B* **2002**, *106* (32), 8705–8713.
- (16) Lefèvre, M.; Dodelet, J. P.; Bertrand, P. *J. Phys. Chem. B* **2005**, *109*, 16718–16724.
- (17) Charretier, F.; Jaouen, F.; Ruggeri, S.; Dodelet, J. P. *Electrochim. Acta* **2008**, *53*, 2925–2938.
- (18) Lalande, G.; Côté, R.; Tamizhmani, G.; Guay, D.; Dodelet, J. P.; Dignard-Bailey, L.; Weng, L. T.; Bertrand, P. *Electrochim. Acta* **1995**, *40* (16), 2635–2646.
- (19) Faubert, G.; Lalande, G.; Côté, R.; Guay, D.; Dodelet, J. P.; Weng, L. T.; Bertrand, P.; Dénès, G. *Electrochim. Acta* **1996**, *41* (10), 1689–1701.
- (20) Faubert, G.; Côté, R.; Guay, D.; Dodelet, J. P.; Dénès, G.; Poleunis, C.; Bertrand, P. *Electrochim. Acta* **1998**, *43* (14–15), 1969–1984.
- (21) Johnston, C. M.; Piela, P.; Zelenay, P. In *Handbook of Fuel Cells – Fundamentals, Technology and Applications*; Vielstich, W.; Yokokawa, H.; Gasteiger, H. A., Eds.; John Wiley & Sons: New York, 2009; Vol. 5, Chapter 4.
- (22) Feng, Y.; Alonso-Vante, N. *Phys. Status Solidi B* **2010**, *245* (9), 1792–1806.
- (23) Gewirth, A. A.; Thorum, M. S. *Inorg. Chem.* **2010**, *49*, 3557–3566.
- (24) Kramm, U. I.; Bogdanoff, P.; Fiechter, S. In *Encyclopedia of Sustainability Science and Technology*; Meyers, R. A., Ed.; Springer: Berlin, 2012.
- (25) Choi, H. J.; Kwag, G.; Kim, S. *J. Electroanal. Chem.* **2001**, *508*, 105–114.
- (26) Bambagioni, V.; Bianchini, C.; Filippi, J.; Lavacchi, A.; Oberhauser, W.; Marchionni, A.; Moneti, S.; Vizza, F.; Psaro, R.; Dal Santo, V.; et al. *J. Power Sources* **2011**, *196*, 2519–2529.
- (27) Alves, M. C. M.; Dodelet, J. P.; Guay, D.; Ladouceur, M.; Tourillon, G. *J. Phys. Chem.* **1992**, *96*, 10898–10905.
- (28) Bouwkamp-Wijnoltz, A. L.; Visscher, W.; van Veen, J. A. R.; Tang, S. C. *Electrochim. Acta* **1999**, *45*, 379–386.
- (29) Herrmann, I.; Bogdanoff, P.; Schmithals, G.; Fiechter, S. *ECS Trans.* **2006**, *3* (1), 211–219.
- (30) Teliska, M.; O'Grady, W. E.; Ramaker, D. E. *J. Phys. Chem. B* **2005**, *109*, 8076–8084.
- (31) Ziegelbauer, J. M.; Olson, T. S.; Pylypenko, S.; Alamgir, F.; Jaye, C.; Atanassov, P.; Mukerjee, S. *J. Phys. Chem. C* **2008**, *112*, 8839–8849.
- (32) Lima, F. H. B.; Calegari, M. L.; Ticianelli, E. A. *Electrochim. Acta* **2007**, *52*, 3732–3738.
- (33) Baturina, O. A.; Gould, B. D.; Korovina, A.; Garsany, Y.; Stroman, R.; Northrup, P. A. *Langmuir* **2011**, *27*, 14930–14939.
- (34) Prietzel, J.; Botzaki, A.; Tyufekchieva, N. *Environ. Sci. Technol.* **2011**, *45*, 2878–2886.
- (35) Hyde, T. I.; Ash, P. W.; Boyd, D. A.; Randlshofer, G.; Rothenbacher, K.; Sankar, G. *Platinum Met. Rev.* **2011**, *55* (4), 233–245.
- (36) Kim, K.; Zhu, P.; Li, N.; Ma, X.; Chen, Y. *Carbon* **2011**, *49*, 1745–1751.
- (37) Schulenburg, H.; Stankov, S.; Schünemann, V.; Radnik, J.; Dorbandt, I.; Fiechter, S.; Bogdanoff, P.; Tributsch, H. *J. Phys. Chem. B* **2003**, *107*, 9034–9041.

- (38) Kramm, U. I.; Abs-Wurmbach, I.; Herrmann-Geppert, I.; Radnik, J.; Fiechter, S.; Bogdanoff, P. *J. Electrochem. Soc.* **2011**, *158* (1), B69–B78.
- (39) Ravel, B.; Newville, M. *J. Synchrotron Radiat.* **2005**, *12*, 537–541.
- (40) Ha, S. H.; Ohta, T.; Kwag, G.; Kim, S. *Electrochem. Solid-State Lett.* **1999**, *2* (9), 461–464.
- (41) Campos, A.; Lohitharn, N.; Roy, A.; Lotero, E.; Goodwin, J. G., Jr.; Spivey, J. J. *Appl. Catal., A* **2010**, *375*, 12–16.
- (42) Kopelev, N. S.; Chechersky, V.; Nath, A.; Wang, Z. L.; Kuzmann, E.; Zhang, B.; Via, G. H. *Chem. Mater.* **1996**, *7*, 1419–1421.
- (43) Scherson, D.; Tanaka, A. A.; Gupta, S. L.; Tryk, D.; Fierro, C.; Holze, R.; Yeager, E. B. *Electrochim. Acta* **1986**, *31* (10), 1247–1258.
- (44) Koslowski, U. I.; Herrmann, I.; Bogdanoff, P.; Barkschat, C.; Fiechter, S.; Iwata, N.; Takahashi, H.; Nishikori, H. *ECS Trans.* **2008**, *13* (17), 125–141.
- (45) Faubert, G.; Côté, R.; Dodelet, J. P.; Lefèvre, M.; Bertrand, P. *Electrochim. Acta* **1999**, *44*, 2589–2603.
- (46) Wei, G.; Wainright, J. S.; Savinell, R. F. *J. New Mater. Electrochem. Syst.* **2000**, *3*, 121–129.
- (47) Herrmann, I.; Kramm, U. I.; Radnik, J.; Fiechter, S.; Bogdanoff, P. *J. Electrochem. Soc.* **2009**, *156* (10), B1283–B1292.
- (48) Kramm (née Koslowski), U. I.; Herrmann, I.; Fiechter, S.; Zehl, G.; Zizak, I.; Abs-Wurmbach, I.; Radnik, J.; Dorbandt, I.; Bogdanoff, P. *ECS Trans.* **2009**, *25* (1), 659–670.
- (49) Kobayashi, M.; Niwa, H.; Saito, M.; Harada, Y.; Oshima, M.; Ofuchi, H.; Terakura, K.; Ikeda, T.; Koshigoe, Y.; Ozaki, J. I.; et al. In Proceedings of the 216th ECS Meeting, Vienna Austria, Oct 2009.
- (50) van Wingerden, B.; van Veen, J. A. R.; Mensch, C. T. J. *J. Chem. Soc., Faraday Trans. 1* **1988**, *84* (1), 65–74.
- (51) Faubert, G.; Côté, R.; Guay, D.; Dodelet, J. P.; Dénès, G.; Bertrand, P. *Electrochim. Acta* **1998**, *43* (3–4), 341–353.
- (52) Côté, R.; Lalonde, G.; Guay, D.; Dodelet, J. P.; Dénès, G. *J. Electrochem. Soc.* **1998**, *145* (7), 2411–2418.
- (53) Greenwood, N. N.; Gibb, T. C. *Mössbauer Spectroscopy*, 1st ed.; Chapman and Hall: London, 1971; Vol. 1.
- (54) Andres, H.; Bominaar, E. L.; Smith, J. M.; Eckert, N. E.; Holland, P. L.; Münck, E. J. *Am. Chem. Soc.* **2002**, *124* (12), 3012–3025.
- (55) Taube, R. *Pure Appl. Chem.* **1974**, *38*, 427–438.
- (56) Debrunner, P. G. In *Iron Porphyrins Part III*; Lever, A. B. P., Gray, H. B., Eds.; VCH Publishers Inc.: New York, 1989.
- (57) Peev, T.; Taseva, V.; Akala, A. *Werkst. Korros.* **1993**, *44*, 62–65.
- (58) Borsa, D. M.; Boerma, D. O. *Hyperfine Interact.* **2003**, *151/152*, 31–48.
- (59) Gajbhiye, N. S.; Panda, R. N.; Ningthoujam, R. S.; Bhattacharyya, S. *Phys. Status Solidi C* **2004**, *1*, 3449–3454.
- (60) Audier, M.; Bowen, P.; Jones, W. J. *Cryst. Growth* **1983**, *64*, 291–296.
- (61) Kramm, U. I. PhD Thesis, Technische Universität Berlin, 2009; <http://opus.kobv.de/tuberlin/volltexte/2009/2287/>.
- (62) Grabke, H. J.; Moszynski, D.; Muller-Lorenz, E. M.; Schneider, A. *Surf. Interface Anal.* **2002**, *34*, 369–374.
- (63) Lalonde, G.; Côté, R.; Guay, D.; Dodelet, J. P.; Weng, L. T.; Bertrand, P. *Electrochim. Acta* **1997**, *42* (9), 1379–1388.
- (64) Jaouen, F.; Lefèvre, M.; Dodelet, J. P.; Cai, M. *J. Phys. Chem. B* **2006**, *110* (11), 5553–5558.
- (65) Jaouen, F.; Herranz, J.; Lefèvre, M.; Dodelet, J. P.; Kramm, U. I.; Herrmann, I.; Bogdanoff, P.; Maruyama, J.; Nagaoka, T.; Garsuch, A.; et al. *ACS Appl. Mater. Interfaces* **2009**, *1* (8), 1623–1639.
- (66) Lefèvre, M.; Proietti, E.; Jaouen, F.; Dodelet, J. P. *Science* **2009**, *324*, 71–74.
- (67) Wang, H.; Ct, R.; Faubert, G.; Guay, D.; Dodelet, J. P. *J. Phys. Chem. B* **1999**, *103* (12), 2042–2049.
- (68) Jaouen, F.; Marcotte, S.; Dodelet, J. P.; Lindbergh, G. *J. Phys. Chem. B* **2003**, *107* (6), 1376–1386.
- (69) Pels, J. R.; Kapteijn, F.; Moulijn, J. A.; Zhu, Q.; Thomas, K. M. *Carbon* **1995**, *33*, 1641–1653.
- (70) Karweik, D. H.; Winograd, N. *Inorg. Chem.* **1976**, *15*, 2336–2342.
- (71) Artyushkova, K.; Halevi, B.; Serov, A.; Atanasov, P.; Ramaswamy, N.; Mukerjee, S. Presented at the 220th ECS Meeting, Boston, MA, October 2011.
- (72) Ding, Z.; Johnston, C. M.; Zelenay, P. *ECS Trans.* **2010**, *33* (1), 565–577.
- (73) Herrmann, I. PhD Thesis, Freie Universität Berlin 2006; http://www.diss.fu-berlin.de/diss/receive/FUDISS_thesis_000000002133.
- (74) Jaouen, F.; Proietti, E.; Lefèvre, M.; Chenitz, R.; Dodelet, J. P.; Wu, G.; Chung, H. T.; Johnston, C. M.; Zelenay, P. *Energy Environ. Sci.* **2011**, *4* (1), 114–130.
- (75) Ferrandon, M.; Wang, X.; Kropf, A. J.; Myers, D. J.; Wu, G.; Johnston, C. M.; Zelenay, P., to be published.